

Short Communication

(Co_{0.94}Fe_{0.06})₃O₄ Nanoparticles Embedded Porous Hollow Carbon Nanowire Derived from Co-based metal-organic Frameworks and Its Capacitive Behavior

Wei Guo^{1,*}, Yinyu Xiang², Yijing Xing¹, Shang Li¹, Junsheng Li², Haolin Tang^{1,*}

¹ State Key Laboratory of Advanced Technology for Materials Synthesis and Processing, Wuhan University of Technology, Luoshi Road 122#, Wuhan 430070, PR China

² Department of Chemistry, Chemical Engineering and Life Sciences, Wuhan University of Technology, Luoshi Road 122#, Wuhan 430070, PR China

*E-mail: tanghaolin2005@yahoo.com.cn, 12239@whut.edu.cn

Received: 31 July 2016 / Accepted: 12 September 2016 / Published: 1 October 2016

In this work, (Co_{0.94}Fe_{0.06})₃O₄ nanoparticles embedded porous hollow carbon nanowire were prepared by a low temperature calcinations of Co₂(BDC)₂(dabco) powder loaded with Fe³⁺ ions. The overall morphology of the MOF material was largely maintained after this low temperature calcinations process. The morphological and compositional characteristics of the calcination products are investigated. It is found that the calcination leads to the generation of (Co_{0.94}Fe_{0.06})₃O₄ nanoparticles decorated porous carbon hollow nanowire. The supercapacitance behavior of the (Co_{0.94}Fe_{0.06})₃O₄ nanoparticles decorated porous carbon hollow nanowire was also explored.

Keywords: Metal Organic Framework, (Co_{0.94}Fe_{0.06})₃O₄, Nanowire, Supercapacitor, Porous carbon

1. INTRODUCTION

Supercapacitor,[1-3] as an important energy-storage device that has fast charge-discharge capability, long cycle life, and high power density, finds a wide range of applications in some key areas, such as portable power source, emergency power supply, and electric vehicle. Among the numerous supercapacitor materials under investigation, much attention has been paid to metal oxide materials,[4, 5] especially Co₃O₄nanomaterials.[6, 7] Co₃O₄ nanomaterial has been studied widely as a promising capacitive material because of its high reversible redox reactions, low cost and environmental friendliness. However, in contrast to other commonly used supercapacitor materials, the capacitance performance and long-term stability of the Co₃O₄ synthesized by conventional methods is still need to improved.[8] One of the reasons for this is that most of the reported Co₃O₄ nanostructures

has poorly controlled morphology. Therefore, exploration of novel Co_3O_4 nanostructures is demanded for an efficient Co_3O_4 based supercapacitor.

A very appealing strategy to reach this goal is the synthesis of metal oxide hybrid nanomaterial, such as $\text{Co}_3\text{O}_4/\text{Ni}(\text{OH})$ composite[9] or $\text{Co}_3\text{O}_4@\text{Ni-Co-O}$ composite.[10] Such hybrid nanomaterials take the advantages of the both component and thus show a wide electrochemical window and high capacitive performance. Besides the compositional characteristics of the metal oxide material, another main factor that influences the pseudocapacitive performance of Co_3O_4 nanomaterial is its morphology, which is directly determined by its synthetic strategy. Up to now, lots of synthetic strategies have been developed to fabricate these hybrid nanomaterials, such as the self-supported hydrothermal synthesis,[6] anodic aluminum oxide (AAO) template synthesis,[11] electrochemical deposition,[9] and metal organic frameworks (MOFs) template synthesis.[12-14] MOFs, which have emerged as an extensive class of crystalline materials with ordered and nanoscale topography, was widely researched recently.[15, 16] These crystalline and nanoporous MOF materials are formed by mixing two essential building blocks, namely, metal ions (inorganic units) and organic ligands. This special structure greatly promotes creative, nimble and flexible of MOFs, resulting in more than 20,000 MOF structures, such as HKUST-1, MOF-5 and ZIF-8 since the first MOF material was reported in 1995.[17] This kind of material is widely applied in catalysis,[18] gas adsorption,[19] biomedicine,[20] chemical sensors[21] and supercapacitor.[22]

In this work, we first used the solvothermal technique to fabricate a layer-pillar-type CoMOF [$\text{Co}_2(\text{BDC})_2(\text{dabco})$: BDC, 1,4-dicarboxybenzene acid (Figure S1a); dabco, 1,4-Diazabicyclo[2.2.2]octane (Figure S1b)] nanowire structure material. CoMOF was further loaded with $\text{Fe}(\text{NO}_3)_3$ and then the composite was used as precursor for the low temperature calcination. Upon calcination, $(\text{Co}_{0.94}\text{Fe}_{0.06})_3\text{O}_4$ nanoparticles encapsulated porous hollow material with nanowire structure [$(\text{Co}_{0.94}\text{Fe}_{0.06})_3\text{O}_4@\text{CON}$] was successfully obtained. Lots of $(\text{Co}_{0.94}\text{Fe}_{0.06})_3\text{O}_4$ nanoparticles are distributed uniformly inside or on the surface of this porous hollow structure material. The electrochemical tests demonstrated that this novel material had a large specific capacitance of $169 \text{ F}\cdot\text{g}^{-1}$ at $1 \text{ A}\cdot\text{g}^{-1}$, which show a highly promising electrode material for supercapacitor applications.

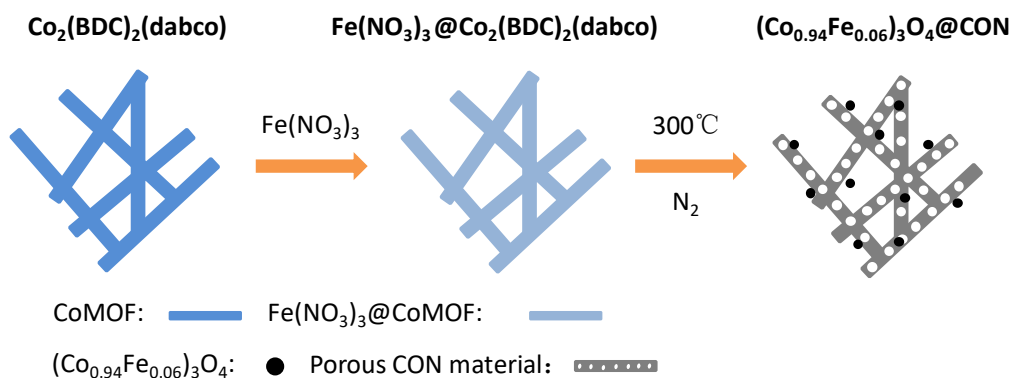


Figure 1. Synthesis scheme of $(\text{Co}_{0.94}\text{Fe}_{0.06})_3\text{O}_4$ nanoparticles embedded porous hybrid material.

2. EXPERIMENTAL AND CHARACTERIZATION

2.1 Fabrication of $\text{Co}_2(\text{BDC})_2(\text{dabco})$

The $\text{Co}_2(\text{BDC})_2(\text{dabco})$ was fabricated by solvothermal technique. A mixture of $\text{Co}(\text{Ac})_2 \cdot 6\text{H}_2\text{O}$ (Sigma, 99%) (0.611 g, 2.10 mmol), H_2BDC (Sigma, 99%) (0.349 g, 2.10 mmol), and dabco (Sigma, 99%) (0.117 g, 1.04 mmol) was dissolved in deionizer water (25 mL) and heated in a 50 mL flask at 80°C for 1 day. The blue crystalline precipitate formed (Figure S2a) was collected, washed with deionizer water, and dried under reduced pressure at room temperature for 2 h.

2.2 Loading of $\text{Fe}(\text{NO}_3)_3$ into the $\text{Co}_2(\text{BDC})_2(\text{dabco})$

Firstly, the fresh $\text{Co}_2(\text{BDC})_2(\text{dabco})$ (0.5 g) powder was put into 250ml flask. And then, the flask was evacuated to 0.2 KPa at room temperature for 30min. Subsequently, the sample was immersed in a freshly prepared solution of $\text{Fe}(\text{NO}_3)_3$ in deionizer water kept at 65°C . After an immersion time of 12h, the sample was removed from the solution, rinsed with deionizer water, for three times, and dried under reduced pressure at room temperature for 2 h, finally the light blue crystalline powder was collected.

2.3 Preparation of the $(\text{Co}_{0.94}\text{Fe}_{0.06})_3\text{O}_4@ \text{CON}$

$\text{Fe}(\text{NO}_3)_3@ \text{Co}_2(\text{BDC})_2(\text{dabco})$ powder were heated in a high temperature furnace with N_2 protection from room temperature to 300°C , the heating rate is 5°C per min and maintained at 300°C for 1 hour, finally the black powder was collected.

2.4 Preparation of the electrode

The working electrodes were prepared as follows. The active material $(\text{Co}_{0.94}\text{Fe}_{0.06})_3\text{O}_4@ \text{CON}$, conductive graphite and polytetrafluoroethylene (PTFE) solution (60 wt %) were mixed in a mass ratio 8:1:1 and isopropanol was added to form dough which was rolled into thin film. 13 mm diameter electrodes were cut from the film. After vacuum-dried at 120°C for 4 h, the electrodes were weighted. And then, the obtained electrodes were pressed onto current collectors (nickel foam) under 10 MPa. These electrodes were dried under vacuum at 120°C for 4 h. The mass of the active materials was in the range of 14.4 mg to 16.0 mg.

2.5 Characterizations

X-ray Diffraction (XRD): Each sample was characterized by using a Bruker D8 Advance equipped with a Si-strip detector (PSD Lynxeye©; position sensitive detector) with $\text{Cu K}\alpha_{1,2}$ radiation

($\lambda = 0.15418$ nm) in θ - θ geometry, variable slit on primary circle. Scans were run over from 5° to 60° 2θ angle with step width of 0.024° , for higher order peaks up to 5 seconds per step.

Infrared reflection absorption (IRRA) spectroscopy: all samples were recorded using a Bruker Optics Tensor 27 spectrometer with a Bruker Optics Platinum® ATR accessory and a duterated triglycine sulfate detector. The ATR spectrum was recorded at room temperature with a resolution of 4 cm^{-1} using air as background. Data were processed using Bruker evaluation software OPUS 7.2.

Scanning electron microscope (SEM) and Energy dispersive spectrometer (EDS): All samples were analyzed using a Zeiss HR-SEM (Gemini Class) in combination with EDS microanalysis at 3–5 kV to check the powder of differently prepared (loaded, unloaded and calcination) MOF.

Transmission electron microscopy (TEM): Plane-view measurements have been performed using an image aberration corrected FEI Titan 80-300 operated at 300 kV and equipped with a Gatan US1000 CCD camera for TEM and a Fischione HAADF detector for STEM imaging. The STEM analysis was performed at liquid N_2 temperatures to reduce electron beam damage of the MOF.

All the electrochemical measurements were carried out on account of a three electrode system under normal atmospheric conditions. Furthermore, 1 M KOH was used as an electrolyte solution. Then, a Pt sheet and a saturated calomel electrode (SEC) were used as counter and reference electrode, respectively. Cyclic voltammetry (CV) and electrochemical impedance spectroscopy (EIS) were done using Autolab PGSTAT 320 N electrochemical workstation. Galvanostatic charge-discharge (GCD) was conducted using a CHI660D electrochemical workstation. The voltage window of CV was from -0.2 V to 0.6 V at different scan rates from 2 mVs^{-1} to 100 mVs^{-1} , GCD was measured between 0 and 0.43 V with different current densities from 1 A g^{-1} to 10 A g^{-1} and EIS measurements were performed in a frequency range of 0.01 Hz to 100000 Hz at an open-circuit potential with an amplitude of 5 mV.

3. RESULTS AND DISCUSSION

The synthetic scheme of the $(\text{Co}_{0.94}\text{Fe}_{0.06})_3\text{O}_4$ nanoparticles is shown in Figure 1. In Figure 2, we present XRD data recorded in an out-of-plane geometry for the pristine $\text{Co}_2(\text{BDC})_2(\text{dabco})$ powder (black). According to the experiment data, we found the XRD peaks marked by stars corresponded well to the previous reports,[23] and also matched well with the simulation results (Figure 2 dark yellow). After loading $\text{Fe}(\text{NO}_3)_3$ into Co-MOF, no new diffraction peaks appear or disappear in XRD data (Figure 2 red), revealing that loading the guest molecules does not affect the crystallinity of the host matrix. Moreover, longer immersion times did not lead to a change of its composition, as reflected by the XRD results. The mass loss from dabco ($\text{C}_2\text{H}_4\text{N}^+$) started at 320°C , [23] thus we set the calcinations temperature to be 300°C . After calcinations of the MOF loaded with Fe^{3+} ions at 300°C in N_2 , lots of $(\text{Co}_{0.94}\text{Fe}_{0.06})_3\text{O}_4$ nanoparticles were successfully prepared, which was proved by the XRD data (Figure 2 blue). New peaks appeared at 31.2° and 36.8° (marked by round) match exactly with the pure Co_3O_4 (JCPDS-74-1657) in the (220) and (311) diffraction direction, respectively. This result demonstrates that Fe^{3+} doping in small quantity in Co_3O_4 didn't affect the crystal structure of Co_3O_4 .

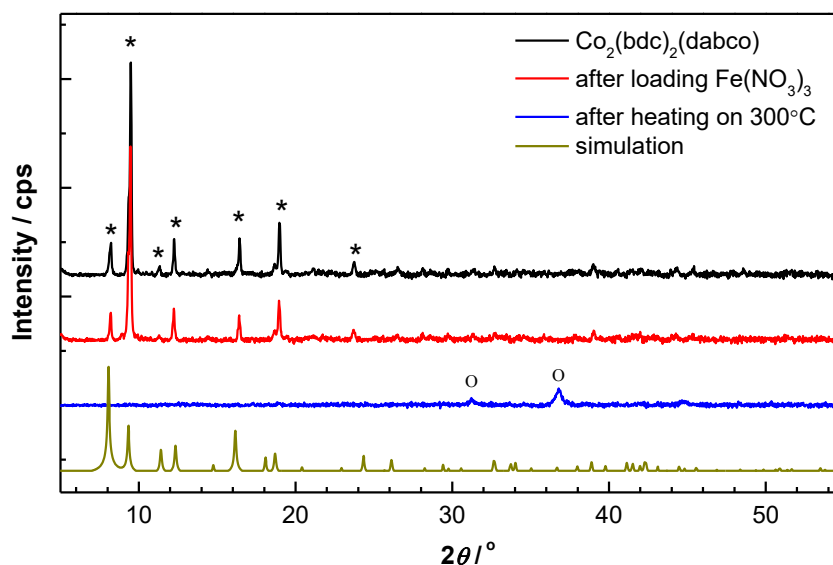


Figure 2. X-ray diffraction patterns recorded: pristine $\text{Co}_2(\text{BDC})_2(\text{dabco})$ (black), after loading $\text{Fe}(\text{NO}_3)_3$ (red), after calcine in N_2 (blue) and simulation (dark yellow).

The morphology of material was examined by SEM and TEM. A typical low-magnification SEM image is shown in Figure 3a (left). The MOF sample showed a uniform, smooth and solid nanowire structure with a diameter of about 100 nm ~ 200 nm (Figure 3a left and Figure S4 left). This morphology of $\text{Co}_2(\text{BDC})_2(\text{dabco})$ is different of the reported in the published results (regular hexahedron microcrystal).[23] To our knowledge, the morphology change of $\text{Co}_2(\text{BDC})_2(\text{dabco})$ has not been reported before. We suspect that the main reason of the morphology change in this case is using $\text{Co}(\text{Ac})_2$ instead of $\text{Co}(\text{NO}_3)_2$. Moreover, the different solvent used in this case was another important factor. The SAED (small area electron diffraction) data (Figure S4 right) had a well-defined diffraction pattern which was fully consistent with the (001) and (010) orientation XRD diffraction data.

Elemental analysis from EDS data demonstrate that the pristine MOF sample is made up of Co (2.94%), C (65.83%), N (7.37%) and O (23.87%) (Figure 3a middle). After loading $\text{Fe}(\text{NO}_3)_3$, the morphology of MOF from SEM and TEM images has no obvious changes (Figure 3b left and right). It is demonstrated that loading the guest molecules into the MOF does not affect the crystallinity of the host matrix. The atomic ratio of the MOF after loaded sample is change to Co (2.43%), C (64.91%), N (6.49%), O (26.02%) and Fe (0.14%) (Figure 3b middle). A small quantity of Fe ions has been successful loading into the MOF and the atomic ratio of Co and Fe is 17.35. More interestingly, the overall shape of the MOF was successfully maintained during the process of calcination, but the internal structure has changed greatly (Figure 3c left). Compared with the precursor, we can clearly see the hollow inner structure of the nanowire from SEM picture. Furthermore, the TEM image shown in Figure 3c right (Figure S5) demonstrates that lots of $(\text{Co}_{0.94}\text{Fe}_{0.06})_3\text{O}_4$ nanoparticles has been formed and embedded into the porous and hollow structures composed. The diameter of those nanoparticles in the nanowire was about 10 nm. In additional, the EDS data show the ratio of atomic number is change to Co (12.95%), C (37.32%), N (0.14%), O (48.9%) and Fe (0.7%) (Figure 3c middle). The atomic ratio of Co and Fe is 18.50.

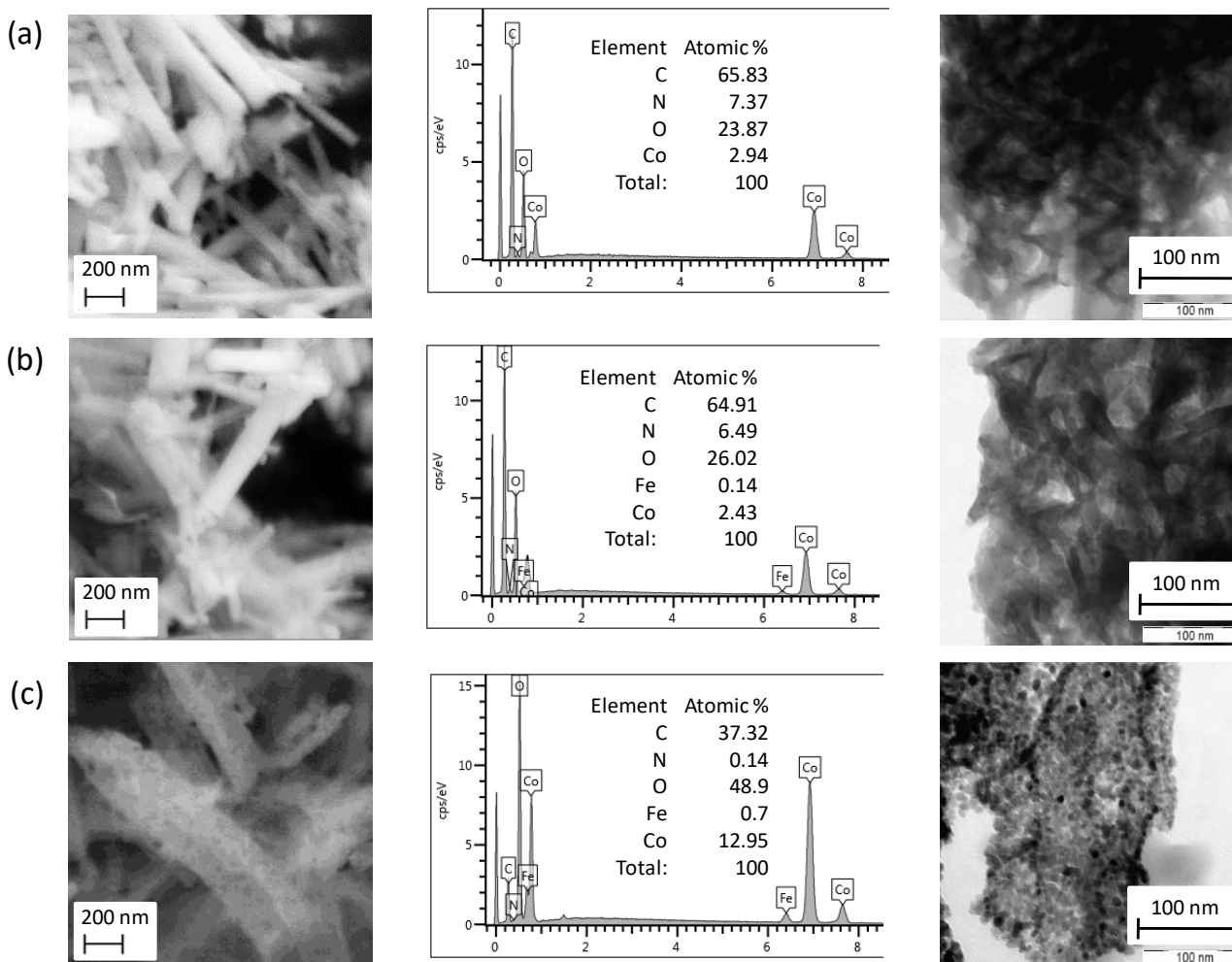
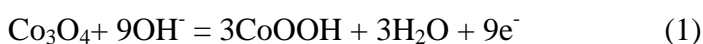


Figure 3. Scanning electron microscopy (SEM) (left), energy dispersive spectrometer (EDS) (middle) and transmission electron microscope (TEM) data of: (a) pristine $\text{Co}_2(\text{BDC})_2(\text{dabco})$; (b) after loading $\text{Fe}(\text{NO}_3)_3$ and (c) calcination of the as prepared precursors in N_2 (blue).

Next, the capacitive performance of the $(\text{Co}_{0.94}\text{Fe}_{0.06})_3\text{O}_4@\text{CON}$ electrode was investigated in 1M KOH solution. Electrochemical impedance spectroscopy (EIS) measurements were first conducted to evaluate the electrical resistance of the electrode. The Nyquist plot was recorded from 0.01 Hz to 100 kHz at open circuit potential (Figure 4a). The internal resistance of the electrode, which can be reflected by the intersection point of the curve with the Z' axis at high frequency region was determined to be 0.83Ω . The charge transfer resistance was calculated to be 0.74Ω . In contrast to the charge transfer resistance of pure Co_3O_4 nanoparticle ($0.80\sim 1.25\Omega$),[24] such a low internal resistance and charge transfer resistance is beneficial for the capacitive performance of the electrode. CV measurements were then performed. A redox pair, which can be assigned to the reversible transition between $\text{Co}^{2+}/\text{Co}^{3+}$ can be clearly observed in the CV curves demonstrating the pseudocapacitive behavior of the electrode (Figure 4b). The surface redox mechanism of Co^{2+} to Co^{3+} according to the following equation (Equation 1):[25]



The pseudocapacitance behavior of the $(\text{Co}_{0.94}\text{Fe}_{0.06})_3\text{O}_4@\text{CON}$ electrode can be clearly seen from the asymmetry nature of the CV curves. As the increase of the scan rate, the oxidation peak shifts positively while the reduction peak shifts negatively which can be caused by the internal resistance of the electrode. A fast charge-discharge response is essential for a high performance supercapacitor. It can be also seen that the peak currents increased with the scan rate, which is indicative of a fast charge-discharge response. Since nanowire structure facilitate the diffusion of ions and electrons,[26] the high charge-discharge response rate of the electrode could be originated from its unique nanowire structure.

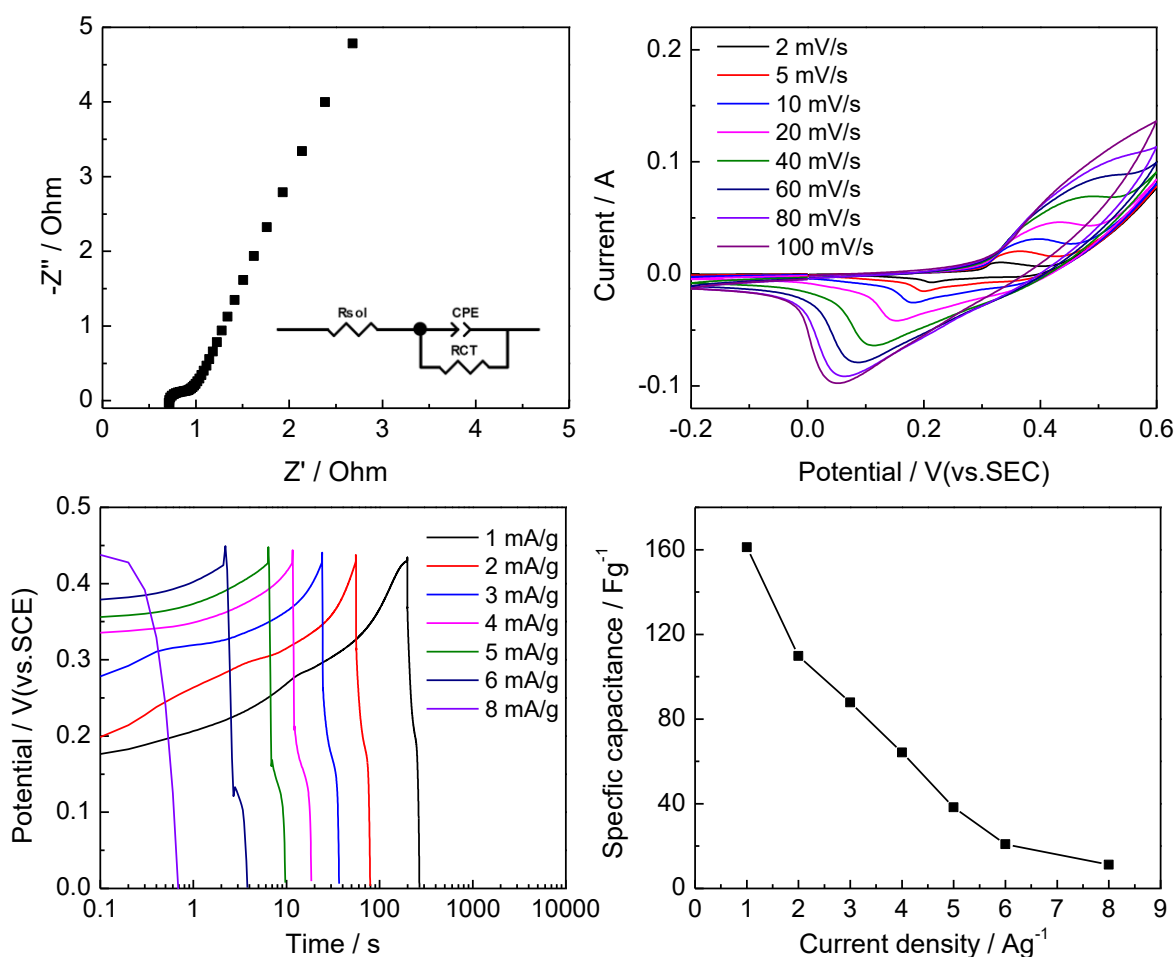


Figure 4. (a) Nyquist plot of the $(\text{Co}_{0.94}\text{Fe}_{0.06})_3\text{O}_4@\text{CON}$ electrode; (b) Cyclic voltammetry curves of the $(\text{Co}_{0.94}\text{Fe}_{0.06})_3\text{O}_4@\text{CON}$ electrode with sweep rates from $2 \text{ mV}\cdot\text{s}^{-1}$ to $100 \text{ mV}\cdot\text{s}^{-1}$; (c) Galvanostatic charge and discharge curves of the $(\text{Co}_{0.94}\text{Fe}_{0.06})_3\text{O}_4@\text{CON}$ electrode at a current density ranging from $1 \text{ A}\cdot\text{g}^{-1}$ to $8 \text{ A}\cdot\text{g}^{-1}$; (d) The specific capacity of the $(\text{Co}_{0.94}\text{Fe}_{0.06})_3\text{O}_4@\text{CON}$ electrode at different current density.

To investigate the capacitance of the electrode, galvanostatic charge-discharge measurements were carried out. The galvanostatic charge-discharge curves of the electrodes at different current density were shown in Figure 4c. The slope of the discharge curve changes at a potential of $\sim 0.22 \text{ V}$,

suggesting the pseudocapacitance behavior of the electrode resulted from the redox reaction at the surface of the electrode. The specific capacitance of the electrode was calculated with the following equation (Equation 2), with I being the current of the charge-discharge process; t being the time of the charge-discharge process; m being the mass of the electrode; ΔV being the electrochemical potential window.

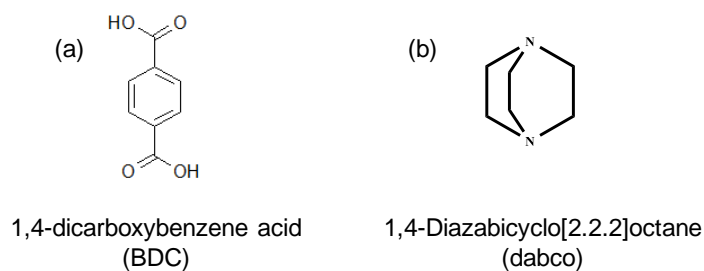
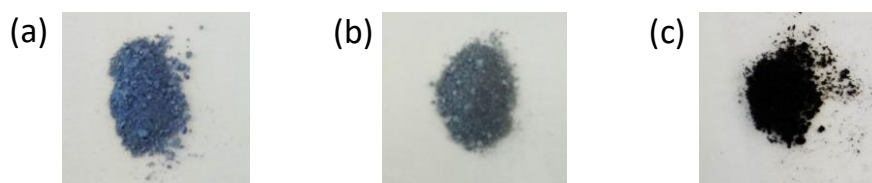
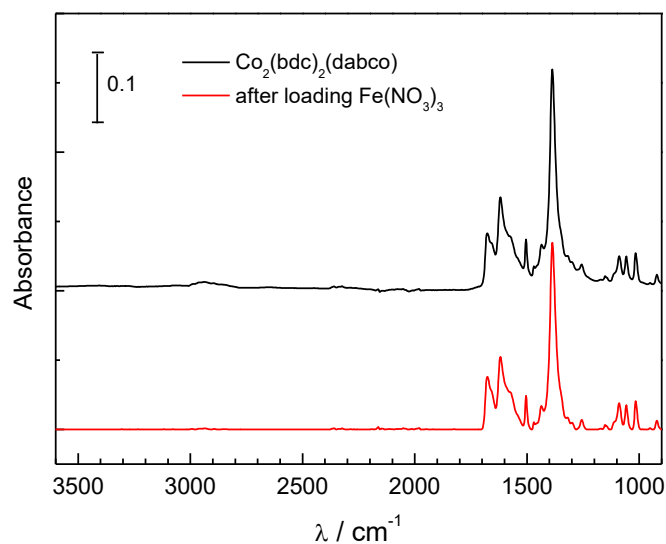
$$C = \frac{It}{m\Delta V} \quad (2)$$

The specific capacity of the electrode was calculated to be 161.2, 109.8, 87.9, 64.2, 38.4, 20.9 and 11.2 F g⁻¹ at 1, 2, 3, 4, 5, 6, 8 A · g⁻¹, respectively (Figure 4d). It should be noted that the fabrication process of these nanostructures generally involves a number of steps or requires finely control over the synthetic conditions. Although the (Co_{0.94}Fe_{0.06})₃O₄@CON electrode reported herein showed lower capacitance than some of the transition metal oxide based supercapacitor reported previously,[27-29] the (Co_{0.94}Fe_{0.06})₃O₄@CON electrode was fabricated through a low cost and simple pyrolysis process, which is highly beneficial for the widespread practical application of the material. To further assess the viability of the (Co_{0.94}Fe_{0.06})₃O₄@CON electrode, cycling stability tests were performed. The measurements were performed at a current density of 2 A · g⁻¹ between 0 V to 0.43 V. As shown in Figure S6, the capacity retention for the electrode reached 67.8 F · g⁻¹, corresponding to a retention ratio of ~60% after 2000 cycles, proving the excellent performance of the electrode. Such a cycling stability is similar to other supercapacitors based on transition metal oxide.[30] Both the nanowire structure and the presence of carbon species on the nanowire helps to release the stress generated during the charge-discharge process, thus help to improve the cycling stability of the electrode.

4. CONCLUSION

In summary, (Co_{0.94}Fe_{0.06})₃O₄ nanoparticles embedded porous hollow nanowire material has been prepared by carbonization of Fe ions loaded Co-based metal-organic frameworks. We show that the Co₃O₄ hybrid nanowire could be readily obtained by appropriate use of precursors, which reveals the importance of precursor for the morphology of the resulting materials. Furthermore, we demonstrate that the carbonization temperature of the MOF precursor also has a profound impact on the morphology of products. The XRD results verified the formation of Co₃O₄ nanoparticles after the carbonization and the TEM images showed that the nanoparticles were uniformly distributed in the porous hollow nanowire structure. By applying this materials for the electrochemical test, a large specific capacitance of 169 F · g⁻¹ at 1 A · g⁻¹ was achieved, which demonstrated that such material exhibits great potential for the applications in the field of capacitor, electrochemical sensing, and lithium ion batteries. Moreover, due to the versatility of the method to produce the metal oxide nanowire, we expect that our method can find more applications in the future synthesis of nanomaterials with desired morphology.

SUPPORTING INFORMATION:

**Figure S1.** The structure formula of (a) BDC and (b) dabco.**Figure S2.** (a) $\text{Co}_2(\text{BDC})_2(\text{dabco})$ powder; (b) $\text{Fe}(\text{NO}_3)_3@ \text{Co}_2(\text{BDC})_2(\text{dabco})$ powder and (c) $(\text{Co}_{0.94}\text{Fe}_{0.06})_3\text{O}_4@ \text{CON}$ powder.**Figure S3.** IR spectrum for $\text{Cu}_2(\text{BDC})_2(\text{dabco})$ (black) and $\text{Fe}(\text{NO}_3)_3@ \text{Co}_2(\text{BDC})_2(\text{dabco})$ (red) of powder.**Table S1.** Band assignment for the IR spectrum of $\text{Cu}_2(\text{BDC})_2(\text{dabco})$ powder.

Absorption band (cm^{-1})	Assignment
1677 and 1688	(COO ⁻) asymm. stretching
1502	Benzene ring

1381	(COO ⁻) symm. stretching
1088 and 1053	Skeletal (from dabco)
1014	Armoaticδ(CH) opp.

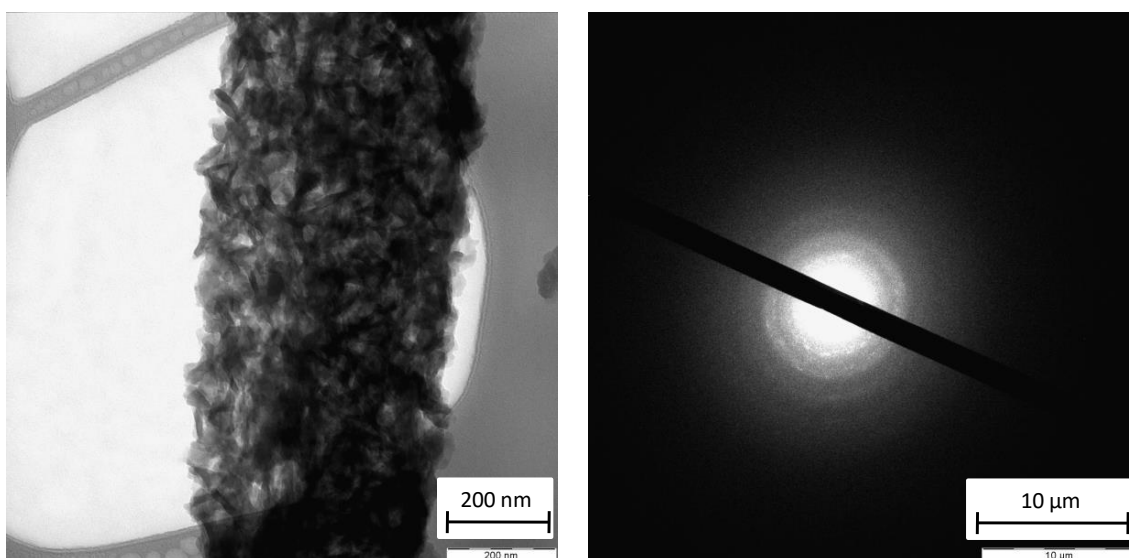


Figure S4. TEM data of $\text{Cu}_2(\text{BDC})_2(\text{dabco})$ (left) and SAED (Selected Area Electron Diffraction) patterns (right).

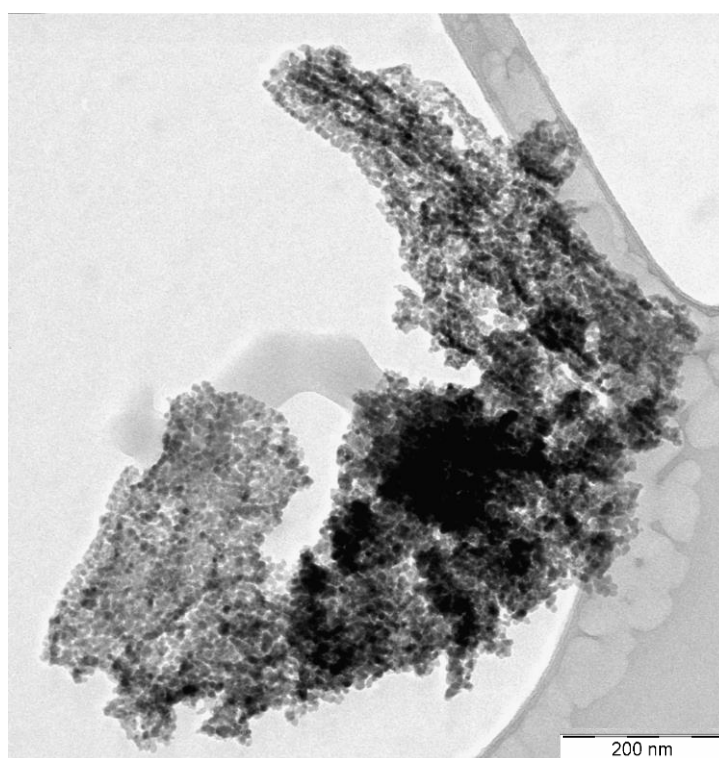


Figure S5. TEM data of $(\text{Co}_{0.94}\text{Fe}_{0.06})_3\text{O}_4@CON$ powder.

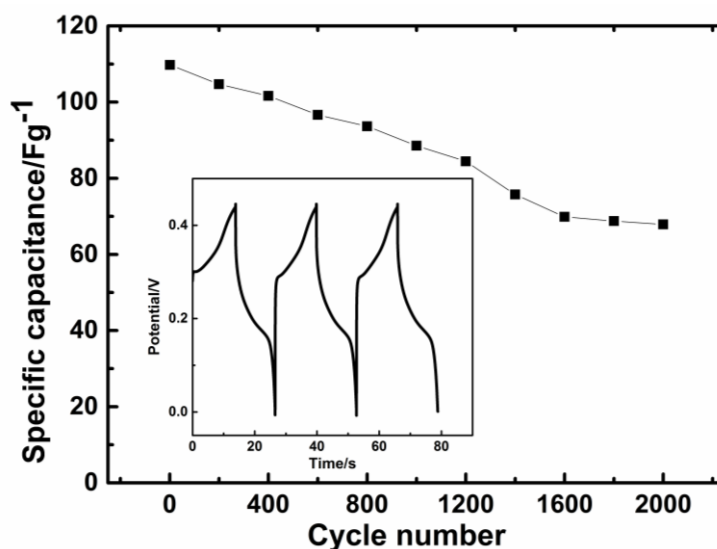


Figure S6. Cycling performance of the $(\text{Co}_{0.94}\text{Fe}_{0.06})_3\text{O}_4@\text{CONElectrode}$ at a current density of 2 A g^{-1} after 2000 cycles.

ACKNOWLEDGEMENT

Financial support by National Natural Science Foundation of China (21406173) is gratefully acknowledged.

References

1. W. F. Wei, X. W. Cui, W. X. Chen and D. G. Ivey, *Chem. Soc. Rev.*, 40 (2011) 1697.
2. L. L. Zhang and X. S. Zhao, *Chem. Soc. Rev.*, 38 (2009) 2520.
3. Y. Wang, Z. Shi, Y. Huang, Y. Ma, C. Wang, M. Chen and Y. Chen, *J. Phys. Chem. C.*, 113 (2009) 13103.
4. H. L. Tang, Y. Zeng, X. Gao, B. Yao, D. Liu, J. B. Wu, D. Y. Qu, K. Liu, Z. Z. Xie, H. N. Zhang, M. Pan, L. Huang and S. P. Jiang, *ElectrochimActa*, 194 (2016) 143.
5. H. Jiang, J. Ma and C. Li, *Adv. Mater.*, 24 (2012) 4197.
6. X. H. Xia, J. P. Tu, Y. J. Mai, X. L. Wang, C. D. Gu and X. B. Zhao, *J. Mater. Chem.*, 21 (2011) 9319.
7. S. K. Meher and G. R. Rao, *J. Phys. Chem. C.*, 115 (2011) 15646.
8. L. Cui, J. Li and X. G. Zhang, *J. Appl. Electrochem.*, 39 (2009) 1871.
9. J. H. Zhong, A. L. Wang, G. R. Li, J. W. Wang, Y. N. Ou and Y. X. Tong, *J. Mater. Chem.*, 22 (2012) 5656.
10. Z. Lu, Q. Yang, W. Zhu, Z. Chang, J. Liu, X. Sun, D. G. Evans and X. Duan, *Nano Res.*, 5 (2012) 369.
11. J. Xu, L. Gao, J. Cao, W. Wang and Z. Chen, *Electrochim. Acta*, 56 (2010) 732.
12. Y. Jiang, L. Chen, H. Zhang, Q. Zhang, W. Chen, J. Zhu and D. Song, *Chem. Eng. J.*, 292 (2016) 1.
13. G. C. Li, X. N. Hua, P. F. Liu, Y. X. Xie and L. Han, *Mater. Chem. Phys.*, 168 (2015) 127.
14. T. Meng, Q. Q. Xu, Z. H. Wang, Y. T. Li, Z. M. Gao, X. Y. Xing and T. Z. Ren, *Electrochim. Acta*, 180 (2015) 104.
15. H. C. Zhou, J. R. Long and O. M. Yaghi, *Chem. Rev.*, 112 (2012) 673.
16. Q. L. Zhu and Q. Xu, *Chem. Soc. Rev.*, 43 (2014) 5468.
17. O. M. Yaghi, G. M. Li and H. L. Li, *Nature*, 378 (1995) 703.

18. A. Dhakshinamoorthy and H. Garcia, *Chem. Soc. Rev.*, 41 (2012) 5262.
19. J. Liu, P. K. Thallapally, B. P. McGrail, D. R. Brown and J. Liu, *Chem. Soc. Rev.*, 41 (2012) 2308.
20. P. Horcajada, R. Gref, T. Baati, P. K. Allan, G. Maurin, P. Couvreur, G. Ferey, R. E. Morris and C. Serre, *Chem. Rev.*, 112 (2012) 1232.
21. L. E. Kreno, K. Leong, O. K. Farha, M. Allendorf, R. P. Van Duyne and J. T. Hupp, *Chem. Rev.*, 112 (2012) 1105.
22. B. Liu, H. Shioyama, H. Jiang, X. Zhang and Q. Xu, *Carbon*, 48 (2010) 456.
23. H. Wang, J. Getzschmann, I. Senkovska and S. Kaskel, *MicroporousMesoporous Mat.*, 116 (2008) 653.
24. K. B. Wang, X. R. Yi, X. F. Luo, S. Yi and J. Y. Xu, *Polyhedron*, 109 (2016) 26.
25. Y. Y. Gao, S. L. Chen, D. X. Cao, G. L. Wang and J. L. Yin, *J. Power Sources*, 195 (2010) 1757.
26. S. L. Zhang and N. Pan, *Adv. Energy Mater.*, 5 (2015) 19.
27. X. H. Lu, Y. X. Zeng, M. H. Yu, T. Zhai, C. L. Liang, S. L. Xie, M. S. Balogun and Y. X. Tong, *Adv. Mater.*, 26 (2014) 3148.
28. M. X. Liu, L. H. Gan, W. Xiong, Z. J. Xu, D. Z. Zhu and L. W. Chen, *J. Mater. Chem. A*, 2 (2014) 2555.
29. Z. M. Hu, X. Xiao, C. Chen, T. Q. Li, L. Huang, C. F. Zhang, J. Su, L. Miao, J. J. Jiang, Y. R. Zhang and J. Zhou, *Nano Energy*, 11 (2015) 226.
30. Z. H. Yang, F. F. Xu, W. X. Zhang, Z. S. Mei, B. Pei and X. Zhu, *J. Power Sources*, 246 (2014) 24.

© 2016 The Authors. Published by ESG (www.electrochemsci.org). This article is an open access article distributed under the terms and conditions of the Creative Commons Attribution license (<http://creativecommons.org/licenses/by/4.0/>).